

LOOC: Localizing Organs using Occupancy Networks and Body Surface Depth Images

Pit Henrich¹ and
Franziska Mathis-Ullrich¹

FAU Erlangen-Nürnberg, Erlangen, Germany
{pit.henrich, franziska.mathis-ullrich}@fau.de
<https://www.sparc.tf.fau.de>

Abstract. We introduce a novel method employing occupancy networks for the precise localization of 67 anatomical structures from single depth images captured from the exterior of the human body. This method considers the anatomical diversity across individuals. Our contributions include the application of occupancy networks for occluded structure localization, a robust method for estimating anatomical positions from depth images, and the creation of detailed, individualized 3D anatomical atlases. This approach promises improvements in medical imaging and automated diagnostic procedures by offering accurate, non-invasive localization of critical anatomical features.

Keywords: Localization of anatomical structures · patient-individual 3D atlas · occupancy networks.

1 Introduction

Multiple medical imaging tasks require an initial location estimate of anatomical structures of interest. For example, an ultrasound probe needs to be positioned such that it visualizes a structure of interest. For Computed Tomography (CT) and Magnetic Resonance Imaging (MRI) a Region of Interest (ROI) needs to be selected on the patient’s body. However, the estimation of anatomical structures is challenging, due to large body shape variability of different people. In practice, medical staff with anatomical understanding and experience must estimate the location of anatomical structures from the outside. In computer-assisted interventions, automatic location estimation of anatomical structures in the human body is an enabler for many down-stream automation tasks and may be performed by non-specialists. In this work we estimate the location, position and scale of human anatomical structures using a single depth image.

Related Work: Medical automation methods, such as robotic ultrasound, often rely on registration methods for path planning [1]. For this, pre-operative CT or MRI data is registered onto the patient body using RGB-D data [12] of the patient skin or the ultrasound image itself for internal structure registration. Both methods require a pre-operatively acquired model.

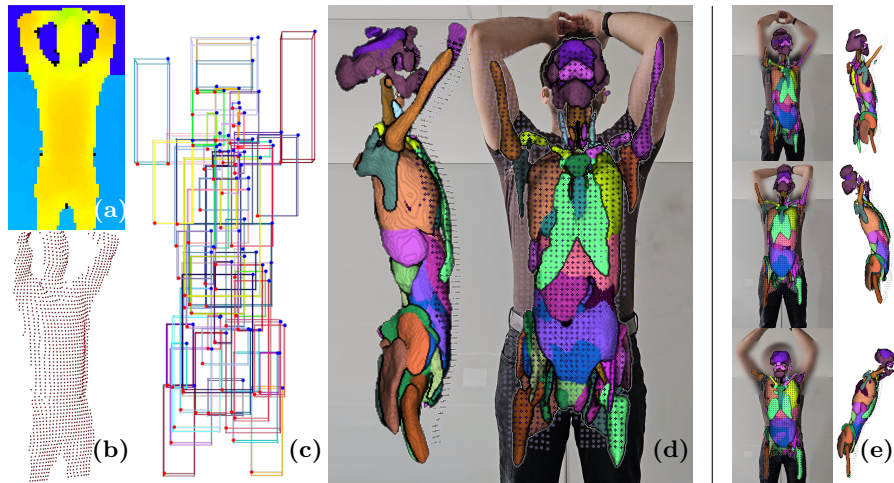


Fig. 1: A depth image (a) is converted to a point cloud (b). Our occupancy network, conditioned on the point cloud, estimates the bounding boxes of 67 anatomical structures (c). It also generates a patient specific 3D anatomical atlas (d). As shown in (e), changing the patient pose also changes the atlas pose.

Rather than registering the patient to a prior scan or template, an atlas based on the point clouds obtained from RGB-D data can be created. The generation of 3D objects based on point clouds experiences a growing interest among researchers. Directly generating surfaces meshes is challenging because of the need for regularizers that ensure good geometry and topology. Convolutional methods [2,4] that generate voxel-based objects suffer from a memory-resolution tradeoff, rendering them unsuitable to the generation of objects with large structures and fine details. DeepSDF [14] and Occupancy Networks [11] represent objects using continuous functions, approximated by neural networks. This enables them to construct both large structures and fine details, without the memory limitations of voxel-based methods. Because occupancy networks use a cross-entropy loss, they are more easily extended to allow the reconstruction of objects with multiple parts. They represent an object by approximating a function which assigns any point in space an *inside* or *outside* value. The boundaries of inside-value-clusters represent a 3D object. Occupancy labels are values assigned to points in 3D space, indicating whether they are inside an object with a value greater than 0 or outside an object with a value equal to 0. An occupancy network is trained using these occupancy labels, where the network needs to predict their labels. The labeling can be conditioned using a secondary input, such as an image or a point cloud.

Henrich et al. [5] demonstrate that single view point clouds can be used to reconstruct deformed objects consisting of multiple parts using a multi-class occupancy function. They propose the use of occupancy networks [11] in combination with PointNet++ [16] to perform a task similar to 3D object registration.

For this, an observation of the deformable object is used to infer a 3D object that best explains this observation. Crucially, the object that is observed is reconstructed. To achieve this, a prior 3D object is deformed to produce both ground truth occupancy samples and sensor-based point clouds. By being presented many combinations of occupancy samples and sensor point clouds, the system learns to label the occupancy samples through supervised learning. The trained network is then queried with a new sensor point cloud and equidistant queries to produce a 3D object.

To train a multi-class occupancy network, 3D objects are needed to generate training data. Several datasets exist for creating human bodies of various shapes and sizes [9,15,13]. The datasets have been applied by Keller et al. [8] to estimate the skeleton shape from an outside image. However, many medical applications focus on other anatomical structures of interest. Jaus et al. presented the Atlas Dataset [7]. Using nnU-Net [6], they produced segmentation masks of 533 human bodies from the AutoPET dataset [3]. These segmentation masks provide location information for 142 anatomical structures.

Contribution: Our contributions are threefold: First, we apply occupancy networks to the task of localizing occluded structures. Second, we provide a method to accurately estimate locations of various anatomical structures from a single depth image. Third, our method produces an estimated 3D anatomical atlas specific to individual patients.

2 Method

We base our method on the 3D deformable object reconstruction by Henrich et al. [5]. However, instead of learning deformation states of a single object, our method learns the morphological diversity of human bodies, such as shape, size, proportion. Further, unlike Henrich et al., our approach does not estimate the seen object’s shape. Instead, we estimate the shape and position of the anatomical structures within the observed object, i.e. the human body.

Henrich et al. [5] use SortSample for their data generation process. SortSample requires segments to have surfaces in contact with the outside. As the inside of the human body is tightly packed, no outside labels exist for internal anatomical structures. We change SortSample such that potential outside labels of a structure are assigned to the neighboring structures’ inside labels. This improvement also resolves a limitation of SortSample by preventing a local bias of segments in contact with each other towards the smaller more densely sampled segment. The remaining hyper-parameters are chosen according to [5].

Training Data: To generate the the training dataset, we use the Atlas Dataset [7] containing anatomical masks for 533 CT scans with a total of 142 distinguishable anatomical structures. For generating the training data, only the masks are needed.

Certain anatomical structures are consistently missing or degenerate across multiple masks. We exclude these structures from our training and evaluation data, including sex-specific organs, such as the ovaries and the prostate. Further,

we grouped the remaining anatomical structures to create more coarse objects. For example, Atlas Dataset separates all vertebrae, which we group into cervical, lumbar, thoracic, and sacrum. After filtering and grouping, 67 anatomical structures remain, see Figure 4. Additionally, 36 masks were removed from the original dataset of 533, due to missing structures. Of the remaining 497 masks, 50 are reserved for evaluation. Therefore, 447 different masks are used for training.

To prepare the Atlas Dataset for our training, we apply the same processing steps to each mask. For each anatomical structure, we obtain a surface-mesh representation using marching cubes [10]. To ensure that all meshes are watertight (i.e., without holes), we add a 1-voxel thick boundary around each mask volume. Atlas Dataset contains some floating regions, wrongly classified. Consequently, for anatomical structures that should form a single connected entity, we select the largest connected mesh. This process effectively eliminates visual floating artifacts. Additionally, we extract the skin surface by grouping all anatomical structures. Notice, performing marching cubes directly on the skin label would result in a mesh with a "thickness", as the inside and the outside of the skin would be converted to surfaces.

To generate a training example, which consists of a point cloud and occupancy sample pair, the following procedure is followed: A random mask is selected. All meshes belonging to the mask are loaded into a virtual scene and a virtual camera is placed at a random distance (meters) $d \sim U(1.4, 2.6)$. Additionally, the camera is moved randomly on the orthogonal plane of the viewing direction by the horizontal and vertical offsets $h \sim U(-7, 7)$ and $v \sim U(-1, 3)$. The camera is then pointed towards the center of the mask. Adjusting the camera position is needed to reflect that the exact distance or relative position of a patient to the camera is often unknown.

A 64×64 depth image is captured of the skin and the modified SortSample is used to obtain 32 inside and 32 outside occupancy samples for each anatomical structure. This excludes the skin itself, which is not reconstructed. The depth image is converted to a point cloud, as we use PointNet++ [16] as an encoder. The occupancy samples are then transformed into the camera space.

A total of 31984 point cloud and occupancy sample pairs are used for training. Early tests on the 447 masks resulted in low generalizability. As a result, real-world data resulted in no organs being reconstructed.

To augment the data and include more diverse poses of the human body, we used a $4 \times 4 \times 4$ lattice based deformation. Each level of the lattice is scaled and rotated to deform the meshes used to produce the training data, see fig. 2. The lattice vertices are positioned such that the middle two levels are at approximately the hip and shoulders. The origin of the rotations and scaling is the geometric center of the lattice level. The rotations are sampled (in degrees) from $U(-15, 15) \times U(-10, 10) \times U(-15, 15)$ for the top and bottom layer. For the middle levels, they are sampled from $U(-5, 5) \times U(-5, 5) \times U(-2.5, 2.5)$. The spatial axes are shown in Figure 2a. The bottom and top most levels are only moved by a small amount, as these affect more rigid structures that should not

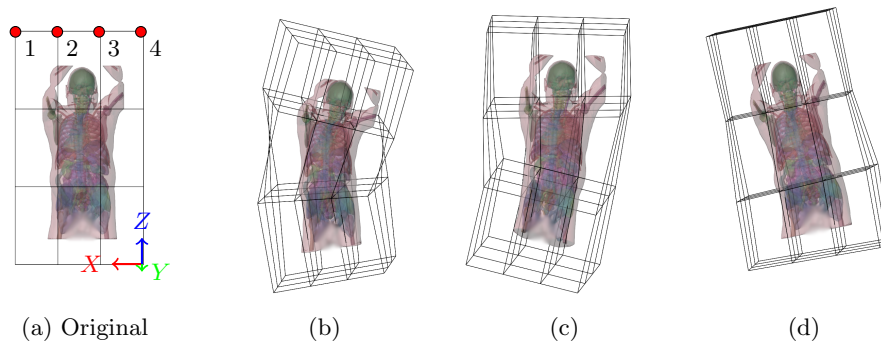


Fig. 2: Examples of the mask data augmentation using a $4 \times 4 \times 4$ lattice (red dots in (a)). The original mask (a) is augmented using the lattice to obtain augmentations (b), (c), and (d).

deform as much, such as the hips. The scaling factor in each level is sampled from $U(0.85, 1.15)$.

As an additional augmentations during training, the point cloud and the occupancy samples are jointly rotated by an angle sampled uniformly in $[-30, 30]$ for each axis. To decrease the sensitivity of point cloud density, we exclude up to 70% of points obtained from the depth image. This reduction also decreases training time, as encoding the point cloud is a bottleneck.

Evaluation Data: As the evaluation dataset, we use the first 50 valid masks without any deformation or rotational augmentation. The camera is placed in a fixed location 1.9 meters from the mask. We compute an Axis Aligned Bounding Box (AABB) for each anatomical structure. This bounding box represents the ROI that we aim to estimate. Some anatomical structures in the Atlas Dataset, such as the ribs and rib cartilage, contain many floating artifacts. As the ribs are not a large connected entity, which allow largest-cluster filtering, these are removed manually to ensure that their AABB are not wrongly scaled.

We collect real-world point clouds of 12 individuals (7 female, 5 male) for a qualitative reconstructions with real-world data. Ages ranged between 26 and 40, height between 154cm and 194cm, weight between 55kg and 97kg. All individuals were fully clothed, but loose clothing was pulled tight. This is in contrast to the training data, where all masks are obtained from individuals without clothing. We use a PMD flexx2 3D Camera (pmdtechnologies ag, Germany). To remove the background, all points further than 2.5 meters are discarded. Finally, the point cloud is cropped, excluding the lower legs and the forearms to match the dataset, see Figure 1. The PMD flexx2 produces denser point clouds than needed, thus, point clouds are sub-sampled randomly until 1000 points remain.

Evaluation Method: For all evaluations, we reconstruct the 3D atlas at a volumetric resolution of $500 \times 500 \times 500$ to ensure small structures are not missed. The atlas is then used to compute the AABB of each anatomical structure for evaluation.

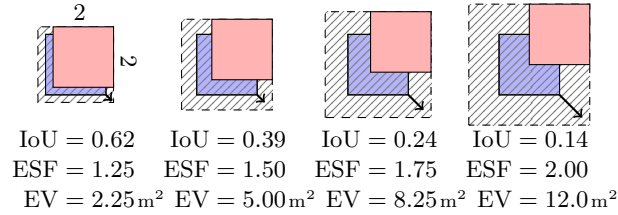


Fig. 3: Visual examples for 2D IoU, ESF and EV. The red box is the target. The blue box is the estimate. Both are $2 \times 2\text{m}$. IoU decreases as the overlap between the boxes decreases. ESF increases as the estimated box needs to be scaled up to encompass the target box. The area of the patterned part is the EV.

We employ three metrics to assess the accuracy of our estimates for the locations of anatomical structures. The AAB B Intersection over Union (IoU) measures the location accuracy of the anatomical structure. For this, the AAB B of each generated anatomical structures is compared against its respective reference bounding box in 3D: $\text{IoU}(A, B) = \text{Volume}(A \cap B) \div \text{Volume}(A \cup B)$.

The Encompassment Scaling Factor (ESF) measures how much the estimated AAB B needs to be scaled such that the reference AAB B is fully contained in it. If the reference is already contained, the ESF is 1. In practice, ESF measures how much an estimated AAB B should be scaled to ensure that the anatomical structure of interest is fully captured by an imaging device during CT or MRI.

We also evaluate the amount of Extra Volume (EV) caused by using the *ESF* enlarged bounding in m^3 : $\text{EV}(A, B) = \text{Volume}(\text{ESF}(A, B) \cdot A) - \text{Volume}(B)$. A visual examples of all metrics are shown in Figure 3.

3 Results and Discussion

All anatomical structures are successfully reconstructed and identified. Quantitative results are presented in Figure 4 and real-world estimated anatomical atlases are qualitatively shown in Figure 5. Generally, the IoU of larger structures, such as the *Liver* (0.62) or the *Colon* (0.64), are higher than of small structures. For small structures, such as the *Gallbladder* or the *Thyroid Left and Right*, small positional offsets (relative to the human size) cause low IoU values of 0.18, 0.05, and 0.11, respectively. These findings are also reflected in the ESF scores, where larger estimated bounding boxes need to be scaled less to encompass the actual structure of interest.

Small structures featuring a small IoU and a high ESF still exhibit a small EV. This occurs because enlarging a small estimated bounding box results in only a minor increase in volume. An exception to both are the *Ribs*, *Rib Cartilage*, and the *Pulmonary Artery*, where poor reconstructions result in a large EV of 0.03, 0.05 and 0.024m^3 . These are complex and space consuming structures and were only assigned 32 inside and 32 outside sample in each training example.

ID	Structure	ID	Structure	ID	Structure	ID	Structure
00	None	17	FemurL	34	IliacVeinR	51	Sacrum
01	AdrenalGlandL	18	FemurR	35	IliopsoasL	52	ScapulaL
02	AdrenalGlandR	19	Gallbladder	36	IliopsoasR	53	ScapulaR
03	Aorta	20	GluteusMaxL	37	InferiorVenaCava	54	Skull
04	ArteryBrachiocephalic	21	GluteusMaxR	38	InternalJugularV.L	55	SmallBowel
05	ArteryInternalCarotidL	22	GluteusMedL	39	InternalJugularV.R	56	Spleen
06	ArteryInternalCarotidR	23	GluteusMedR	40	KidneyL	57	Sternum
07	ArterySubclavianL	24	GluteusMinL	41	KidneyR	58	SternumManubrium
08	ArterySubclavianR	25	GluteusMinR	42	Liver	59	Stomach
09	Bladder	26	Heart	43	LungsL	60	ThyroidL
10	Brain	27	HipL	44	LungsR	61	ThyroidR
11	Cart.CommonCarotidL	28	HipR	45	NasalCavity	62	Trachea
12	Cart.CommonCarotidR	29	HumerusL	46	Pancreas	63	VeinBrachiocephalicL
13	ClavicleL	30	HumerusR	47	Portal&SplenicVein	64	VeinBrachiocephalicR
14	ClavicleR	31	IliacArteryL	48	PulmonaryArtery	65	VertebraeCervical
15	Colon	32	IliacArteryR	49	RibCartilage	66	VertebraeLumbar
16	Esophagus	33	IliacVeinL	50	Ribs	67	VertebraeThoracic

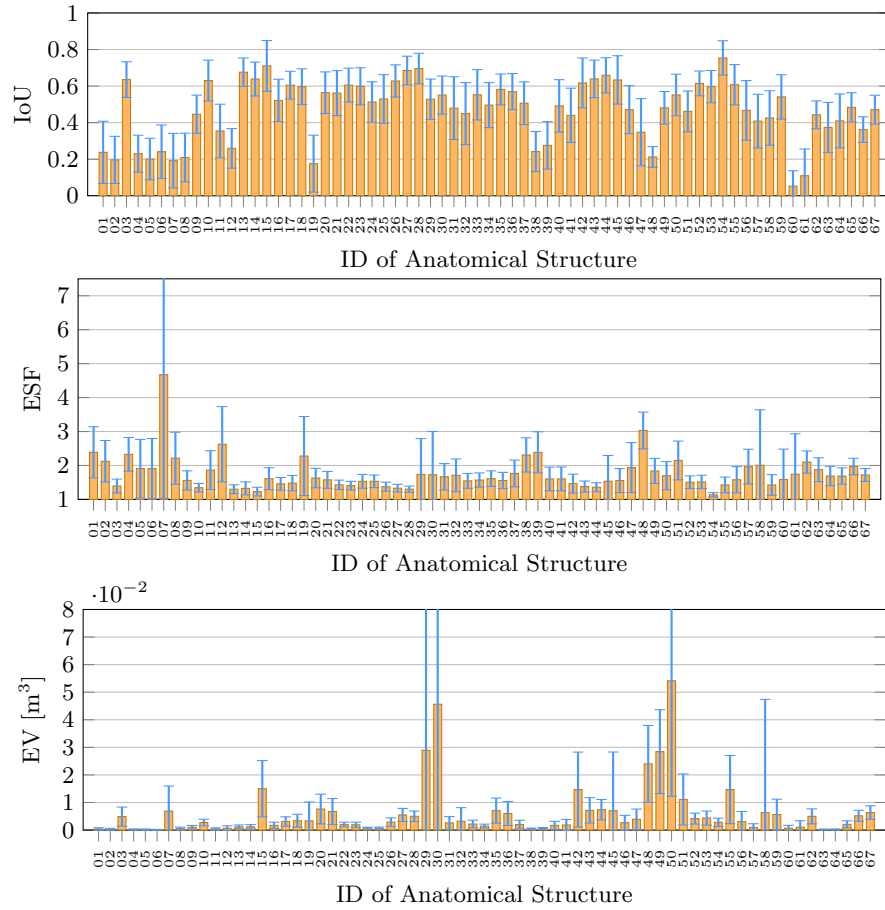


Fig. 4: Table and results of the evaluation on the 50 reserved masks. The table shows the ID for each anatomical structure with suffix L (left) and R (right). The charts show mean IoU, ESF and EV with standard deviation for each anatomical structure. Larger is better for IoU. Smaller is better for EV and ESF.

We suspect that this is an insufficient number of occupancy samples. The error in the reconstruction is illustrated in Figure 5, where the ribs are not correctly reconstructed. Upon visual inspection, the skull suffers from a similar problem as it is a complex thin and hollow structure. Additionally, in many masks used for producing training data, the skull is only partially present. This promotes a partial reconstruction, where the top is open. The *Humerus Left and Right* also have high EV of 0.03 and 0.046 m^3 , respectively. This is likely caused by the arms being truncated in multiple scans, resulting in the occupancy network being uncertain about the correct length of the *humerus*.

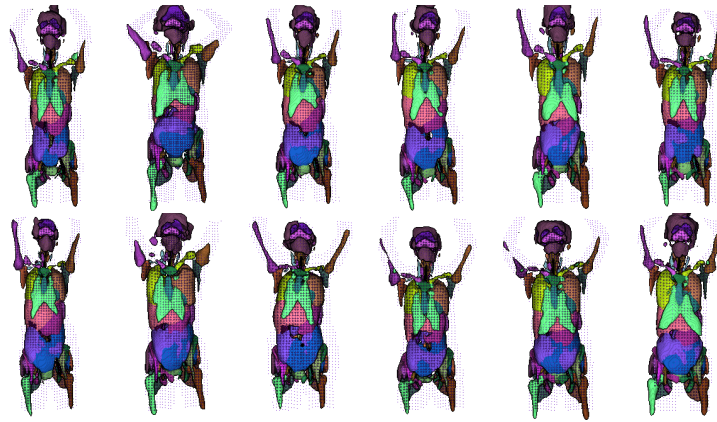


Fig. 5: Reconstructions from real-world data of 12 individuals (7 female, 5 male). The scale of all reconstructions have been normalized for this visualization.

4 Conclusion and Limitations

We present a method that estimates the bounding boxes of 67 anatomical structures in individual human bodies. Trained on augmented virtual data, our system is able to produce an estimated 3D anatomical atlas from a single depth image. We show the accuracy of the system using 50 fully segmented masks excluded from the training dataset. We also provide a real world qualitative overview of 3D atlases of 12 individuals, both males and females.

Despite our method’s accuracy in estimating various anatomical structures, limitations remain: All individuals in the training data have similar poses, where the arms are positioned above the head. As a result, the arms need be positioned similarly during inference. Currently, our method does not provide estimates for sex-specific organs, including reproductive and internal organs. Reconstructions of complex structures are poor, likely caused by too few occupancy samples being used. Our qualitative reconstructions from real-world data was obtained from clothed individuals, whereas the training data only contained individuals

without clothing. The training data misses most of the extremities, such as the lower legs, feet, and hands. AABBs are not the closest fitting bounding boxes, this can result in a sub-optimal region of interest estimate. Finally, we do not provide a comparison to trained medical staff on how they would select the AABB of each anatomical structure.

References

1. Bi, Y., Jiang, Z., Duelmer, F., Huang, D., Navab, N.: Machine learning in robotic ultrasound imaging: Challenges and perspectives. *Annual Review of Control, Robotics, and Autonomous Systems* **7**(1), null (2024). <https://doi.org/10.1146/annurev-control-091523-100042>, <https://doi.org/10.1146/annurev-control-091523-100042>
2. Choy, C.B., Xu, D., Gwak, J., Chen, K., Savarese, S.: 3d-r2n2: A unified approach for single and multi-view 3d object reconstruction. In: *Computer Vision—ECCV 2016: 14th European Conference, Amsterdam, The Netherlands, October 11–14, 2016, Proceedings, Part VIII 14*. pp. 628–644. Springer (2016)
3. Gatidis, S., Hepp, T., Früh, M., La Fougère, C., Nikolaou, K., Pfannenber, C., Schölkopf, B., Küstner, T., Cyran, C., Rubin, D.: A whole-body fdg-pet/ct dataset with manually annotated tumor lesions. *Scientific Data* **9**(1), 601 (2022)
4. Girdhar, R., Fouhey, D.F., Rodriguez, M., Gupta, A.: Learning a predictable and generative vector representation for objects. In: *Computer Vision—ECCV 2016: 14th European Conference, Amsterdam, The Netherlands, October 11–14, 2016, Proceedings, Part VI 14*. pp. 484–499. Springer (2016)
5. Henrich, P., Gyenes, B., Scheikl, P.M., Neumann, G., Mathis-Ullrich, F.: Registered and segmented deformable object reconstruction from a single view point cloud. In: *Proceedings of the IEEE/CVF Winter Conference on Applications of Computer Vision*. pp. 3129–3138 (2024)
6. Isensee, F., Jaeger, P.F., Kohl, S.A., Petersen, J., Maier-Hein, K.H.: nnu-net: a self-configuring method for deep learning-based biomedical image segmentation. *Nature methods* **18**(2), 203–211 (2021)
7. Jaus, A., Seibold, C., Hermann, K., Walter, A., Giske, K., Haubold, J., Kleesiek, J., Stiefelhagen, R.: Towards unifying anatomy segmentation: Automated generation of a full-body ct dataset via knowledge aggregation and anatomical guidelines. *arXiv preprint arXiv:2307.13375* (2023)
8. Keller, M., Zuffi, S., Black, M.J., Pujades, S.: OSSO: Obtaining skeletal shape from outside. In: *Proceedings IEEE/CVF Conf. on Computer Vision and Pattern Recognition (CVPR)*. pp. 20492–20501 (Jun 2022)
9. Loper, M., Mahmood, N., Romero, J., Pons-Moll, G., Black, M.J.: SMPL: A skinned multi-person linear model. *ACM Trans. Graphics (Proc. SIGGRAPH Asia)* **34**(6), 248:1–248:16 (Oct 2015)
10. Lorensen, W.E., Cline, H.E.: Marching cubes: A high resolution 3d surface construction algorithm. In: *Seminal graphics: pioneering efforts that shaped the field*, pp. 347–353 (1998)
11. Mescheder, L., Oechsle, M., Niemeyer, M., Nowozin, S., Geiger, A.: Occupancy networks: Learning 3d reconstruction in function space. In: *Proceedings of the IEEE/CVF conference on computer vision and pattern recognition*. pp. 4460–4470 (2019)

12. Modrzejewski, R., Collins, T., Bartoli, A., Hostettler, A., Marescaux, J.: Soft-body registration of pre-operative 3d models to intra-operative rgbd partial body scans. In: Medical Image Computing and Computer Assisted Intervention–MICCAI 2018: 21st International Conference, Granada, Spain, September 16-20, 2018, Proceedings, Part IV 11. pp. 39–46. Springer (2018)
13. Osman, A.A.A., Bolkart, T., Black, M.J.: STAR: A sparse trained articulated human body regressor. In: European Conference on Computer Vision (ECCV). pp. 598–613 (2020), <https://star.is.tue.mpg.de>
14. Park, J.J., Florence, P., Straub, J., Newcombe, R., Lovegrove, S.: Deepsdf: Learning continuous signed distance functions for shape representation. In: Proceedings of the IEEE/CVF conference on computer vision and pattern recognition. pp. 165–174 (2019)
15. Pavlakos, G., Choutas, V., Ghorbani, N., Bolkart, T., Osman, A.A.A., Tzionas, D., Black, M.J.: Expressive body capture: 3D hands, face, and body from a single image. In: Proceedings IEEE Conf. on Computer Vision and Pattern Recognition (CVPR). pp. 10975–10985 (2019)
16. Qi, C.R., Yi, L., Su, H., Guibas, L.J.: Pointnet++: Deep hierarchical feature learning on point sets in a metric space. *Advances in neural information processing systems* **30** (2017)